Chapter 2
Toward 3D Experimental Impulse-Based Substructuring Using the Virtual Point Transformation

Oliver M. Zobel, Francesco Trainotti, and Daniel J. Rixen

Abstract The application of Impulse-Based Substructuring (IBS) might be advantageous compared to the classical Frequency-Based Substructuring (FBS) approach because it is a time domain method, e.g., allowing for the addition of non-linear elements. In order to be viable for experimental applications, the method must be able to handle real-world systems and interfaces as well as all the experimental issues commonly encountered with substructuring. For this, the Virtual Point Transformation (VPT), commonly used for FBS to model a rigid interface connection, is adapted for use with IBS. With the shown approach, it is possible to correctly reconstruct some of the initial acceleration response peaks of an experimental test-case. The results show that combining a time domain deconvolution, downsampling with low-pass filter, and the VPT fundamentally enables experimental substructuring of three-dimensional structures in the time domain using the IBS method.

Keywords Impulse-based substructuring · Experimental substructuring · Virtual point transformation, · Time domain substructuring · Experimental techniques

Introduction

Impulse-based substructuring (IBS) is the time-domain counterpart of the well-established frequency-based substructuring method (FBS). The IBS method is especially suited for determining shock responses, where the main goal might be to correctly predict the maximum amplitudes, e.g., of the accelerations. Its advantages originate from it being a time-domain method, i.e., high-frequency content, potentially consisting of many modes, can be represented in a short time series. Additionally, since there is no transformation into the frequency domain, there is no forced prioritization, i.e., leakage does not occur.

While this method has been successfully applied for numerical models in the past, see for instance [1–3], experimental applications are just now starting to be conducted. In the authors' previous work [4], it was shown that the IBS method can be used experimentally to determine the initial response peaks of aluminum and polyoxymethylene (POM) rods considered one-dimensional. This was enabled by using a time domain deconvolution procedure to experimentally estimate the impulse response functions (IRF), and additionally, a downsampling approach was proposed for test cases with limited excitation bandwidth, like the POM rods. Whereas this showed that an experimental application of IBS is generally possible, the practical use-cases are limited when only one-dimensional systems or interfaces can be used. Therefore, in this paper, the fundamentals are laid out to apply the IBS method experimentally to three-dimensional systems.

For this, the Virtual Point Transformation (VPT), as proposed in [5], commonly used within FBS to realize experimental six degree of freedom interface coupling, is adapted for the IBS method. The adapted IBS scheme using VPT is then tested experimentally on a substructuring benchmark structure and compared to reference measurements.

Oliver M. Zobel · Francesco Trainotti · Daniel J. Rixen
Chair of Applied Mechanics, TUM School of Engineering and Design, Technical University of Munich, Boltzmannstr. 15, 85748 Garching, Germany
e-mail: oliver.zobel@tum.de; francesco.trainotti@tum.de; rixen@tum.de

Walter D'Ambrogio, et al. (eds.), *Dynamic Substructuring & Transfer Path Analysis, Vol. 4*, Conference Proceedings of the Society for Experimental Mechanics Series, https://doi.org/10.13052/97887-438-0149-8_2

Theory of Impulse-Based Substructuring

Here, only a short summary of the dually assembled Impulse-Based Substructuring (IBS) theory proposed by RIXEN in 2010 in [2] is given. Further details can be found there or in the authors' previous work, 'Enabling Experimental Impulse-Based Substructuring through Time Domain Deconvolution and Downsampling' [4]. The time-continuous IBS method is given by:

Definition Impulse-Based Substructuring Method [2]

$$\begin{cases} \boldsymbol{y}^{(s)}(t) = \displaystyle\int_0^t \boldsymbol{H}^{(s)}(t-\tau)\left(\boldsymbol{f}^{(s)}(\tau) + \boldsymbol{B}_f^{(s)\,\mathrm{T}}\boldsymbol{\lambda}_f(\tau)\right)\mathrm{d}\tau & \text{Equations of Motion} \\ \displaystyle\sum_{s=1}^{N_S} \boldsymbol{B}_y^{(s)}\boldsymbol{y}^{(s)}(t) = \boldsymbol{0} & \text{Compatibility} \end{cases} \tag{1}$$

where:

$\boldsymbol{y}(t)$	System response	$\boldsymbol{H}(t)$	Matrix of impulse response functions	(s)	Substructure index
$\boldsymbol{f}(t)$	Externally applied forces	$\boldsymbol{B}$	Signed Boolean constraint matrix	$*_f$	Force mapping
N_S	Number of substructures	$\boldsymbol{\lambda}(t)$	Global vector of Lagrange multipliers	$*_y$	Response mapping

These equations must be discretized in time, and then a time-marching scheme over the discrete time steps k has to be evaluated. The aforementioned scheme first calculates a prediction of the system responses using a convolution product between the impulse response functions (IRFs) and the applied forces while neglecting the compatibility condition for the current time step k. Then, based on the existing interface gap, Lagrange multipliers $\boldsymbol{\lambda}$ are calculated that, for a linear system, exactly close the gap when applied to the system in the corrector step [2, 4]. This is summarized in fig. 1.

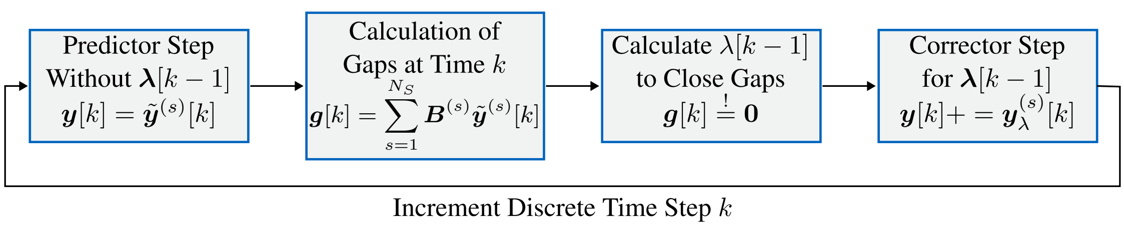

Fig. 1 Flowchart of IBS scheme calculations within each time step

The IRFs are determined from impact measurements using the time domain convolution procedure proposed by [6]. This procedure allows averaging of multiple impacts and essentially is the time domain counterpart of the H_1 FRF estimator.

Depending on the excitation bandwidth compared to the full measurement bandwidth, the system might not be properly excited at all frequencies, see fig. 2. Contrary to FBS, where the higher frequencies can even be omitted after the substructuring procedure, for IBS, the improperly excited frequency content must be removed before the IRF calculation. The authors proposed in [4] to do this with downsampling after applying an appropriate low-pass filter, limiting the considered bandwidth.

Virtual Point Transformation for IBS

For three-dimensional structures, coupling two triaxial sensors on the interface, one on each substructure, is not sufficient as this does not account for the rotational dofs and only couples the three measured translations, while in reality, the interface connection is a line or surface contact, rather than a point contact. Measuring additional rotational dofs is very difficult because the required torque excitation and rotational sensors are not standard measurement equipment [7]. Instead, it was proposed by DE KLERK ET AL. in [7] to determine the rotational dofs by combining multiple triaxial sensors. Nevertheless, this approach was found to be non-ideal, as the interface problem could be overdetermined, and measurement errors can lead to unwanted stiffening and spurious peaks in the coupled FRFs.

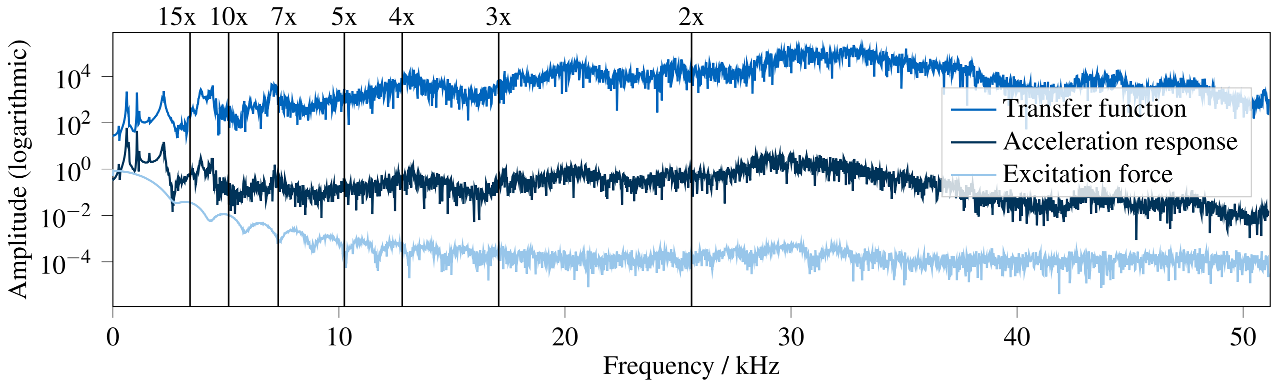

Fig. 2 Example of transfer function calculated from measured acceleration response and excitation signal of the experimental test case; all quantities transformed into the frequency domain. Vertical lines indicate the cut-off point for a downsampling factor as indicated at the top of the line

To solve this problem, the coupling using a virtual point was introduced in [5] by VAN DER SEIJS ET AL.. The interface is assumed to be rigid, i.e., only six rigid body modes, three translations and three rotations, are considered, and the remainder or residual $\boldsymbol{\mu}$ is neglected. The measured interface translations (at least nine) are then projected onto the virtual point with six dofs. This projection weakens the interface coupling and is solved for in a least-square sense, averaging out measurement errors [5].

Projection of Responses For the virtual point transformation, the triaxial sensors are assumed to be rigidly connected to the interface, i.e., the virtual point. The distance from the virtual point to the sensor i is given by the position vector $\boldsymbol{r}_i$, as shown on the left in fig. 3.

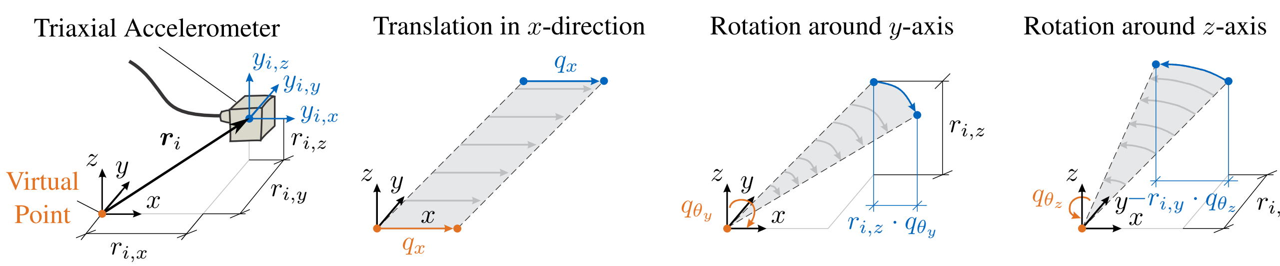

Fig. 3 Projection of triaxial sensor dofs on virtual point exemplarily shown for the measured x-direction $y_{i,x}$ of sensor i, figure adapted from *pyFBS* documentation [8]

Using this vector, the responses $\boldsymbol{y}_i$ measured by the sensor i can be projected onto the virtual point dofs $\boldsymbol{q}$, by deriving the required relations, as exemplary shown for the measured response in the x-direction in fig. 3:

$$\begin{bmatrix} y_{i,x} \\ y_{i,y} \\ y_{i,z} \end{bmatrix} = \begin{bmatrix} 1 & 0 & 0 & 0 & r_{i,z} & -r_{i,y} \\ 0 & 1 & 0 & -r_{i,z} & 0 & r_{i,x} \\ 0 & 0 & 1 & r_{i,y} & -r_{i,x} & 0 \end{bmatrix} \begin{bmatrix} q_x \\ q_y \\ q_z \\ q_{\theta_x} \\ q_{\theta_y} \\ q_{\theta_z} \end{bmatrix} \tag{2}$$

Equation (2), $\boldsymbol{y}_i = \boldsymbol{R}_{y,i}\boldsymbol{q}$ in short notation, describes how the three sensor dofs $\boldsymbol{y}_i$ can be described using the matrix $\boldsymbol{R}_{y,i}$ containing the rigid body modes of sensor i and the reduced virtual point dofs $\boldsymbol{q}$. In case the orientation of the sensor and the virtual point coordinate system does not line up, a rotation matrix has to be added to the equation. Writing this for all n_S sensors and adding a residual $\boldsymbol{\mu}$ to account for the neglected flexible interface motion, the response $\boldsymbol{y}_i$ of all interface sensors is given by [5]:

$$\begin{bmatrix} \boldsymbol{y}_1 \\ \vdots \\ \boldsymbol{y}_{n_S} \end{bmatrix} = \begin{bmatrix} \boldsymbol{R}_{y,1} \\ \vdots \\ \boldsymbol{R}_{y,n_S} \end{bmatrix} \boldsymbol{q} + \boldsymbol{\mu} \tag{3}$$

An optimal solution for the desired virtual point dofs $\boldsymbol{q}$ can then be found by minimizing the residual $\boldsymbol{\mu}$, which yields, without weighting matrices, the desired transformation matrix $\boldsymbol{T}_y$, projecting the measured responses $\boldsymbol{y}$ on the virtual point dofs $\boldsymbol{q}$ [9]:

$$\boldsymbol{T}_y = \left(\boldsymbol{R}_y^{\mathrm{T}} \boldsymbol{R}_y\right)^{-1} \boldsymbol{R}_y^{\mathrm{T}} \qquad \text{with} \qquad \boldsymbol{q} = \boldsymbol{T}_y \boldsymbol{y} \tag{4}$$

Projection of Forces Similar to the projection of the measured responses $\boldsymbol{y}_i$ of sensor i, the forces or impacts $\boldsymbol{f}_i$ applied to the system can be projected onto the virtual point [5]:

$$\begin{bmatrix} m_x \\ m_y \\ m_z \\ m_{\theta_x} \\ m_{\theta_y} \\ m_{\theta_z} \end{bmatrix} = \begin{bmatrix} 1 & 0 & 0 \\ 0 & 1 & 0 \\ 0 & 0 & 1 \\ 0 & -r_{i,z} & r_{i,y} \\ r_{i,z} & 0 & -r_{i,x} \\ -r_{i,y} & r_{i,x} & 0 \end{bmatrix} \begin{bmatrix} e_{i,x} \\ e_{i,y} \\ e_{i,z} \end{bmatrix} f_i \tag{5}$$

where the vector $\boldsymbol{r}_i$ describes the distance between the virtual point and the point where the force is acting and the vector $\boldsymbol{e}_i$ the direction of the scalar force value f_i. Again, all n_I impacts can be combined in one equation $\boldsymbol{m} = \boldsymbol{R}_f^{\mathrm{T}} \boldsymbol{f}$. An optimal solution for the transformation of the virtual point forces $\boldsymbol{m}$ into the physical space of the measured forces $\boldsymbol{f}$ is given by [9]:

$$\boldsymbol{T}_f^{\mathrm{T}} = \boldsymbol{R}_f \left(\boldsymbol{R}_f^{\mathrm{T}} \boldsymbol{R}_f \right)^{-1} \qquad \text{with} \qquad \boldsymbol{f} = \boldsymbol{T}_f^{\mathrm{T}} \boldsymbol{m} \tag{6}$$

Adaption of IBS Equations - Interface Compatibility First, the interface compatibility is no longer written for the physical responses $\boldsymbol{y}^{(s)}$, but for the virtual point dofs $\boldsymbol{q}^{(s)}$ for each virtual point of each substructure s:

$$\sum_{s=1}^{N_S} \boldsymbol{B}_q^{(s)} \boldsymbol{q}^{(s)} = \boldsymbol{0} \qquad \text{with} \qquad \boldsymbol{q}^{(s)} = \begin{bmatrix} q_x^{(s)} & q_y^{(s)} & q_z^{(s)} & q_{\theta_x}^{(s)} & q_{\theta_y}^{(s)} & q_{\theta_z}^{(s)} \end{bmatrix}^{\mathrm{T}} \tag{7}$$

For this, the boolean constrain matrix $\boldsymbol{B}_f^{(s)}$ has to be rewritten for the virtual point dofs $\boldsymbol{q}$ as $\boldsymbol{B}_q^{(s)}$. Inserting the transformation matrix from eq. (4), i.e., $\boldsymbol{q} = \boldsymbol{T}_y \boldsymbol{y}$, gives the interface compatibility condition on the virtual point w.r.t. $\boldsymbol{y}^{(s)}$:

Interface Compatibility on Virtual Point

$$\sum_{s=1}^{N_S} \underset{\left((n_{\mathrm{V}}\cdot 6)\times\left(n_{\mathrm{aS}}^{(s)}+n_{\mathrm{V}}\cdot 6\right)\right)}{\boldsymbol{B}_q^{(s)}} \quad \underset{\left(\left(n_{\mathrm{aS}}^{(s)}+n_{\mathrm{V}}\cdot 6\right)\times n_{\mathrm{S}}^{(s)}\right)}{\boldsymbol{T}_y^{(s)}} \quad \underset{\left(n_{\mathrm{S}}^{(s)}\times 1\right)}{\boldsymbol{y}^{(s)}} = \underset{\left(n_{\mathrm{S}}^{(s)}\times 1\right)}{\boldsymbol{0}} \tag{8}$$

where:

n_{S}	Total number of sensor dofs	n_{V}	Number of Virtual Points	(s)	Substructure index
n_{aS}	Number of additional sensor dofs	N_S	Total number of substructures		

Adaption of IBS Equations - Interface Equilibrium Next, the interface equilibrium has to be written for the virtual point coordinates $\boldsymbol{q}^{(s)}$, i.e., the Lagrange multipliers $\boldsymbol{\lambda}_m$ are applied to the virtual point as virtual forces:

$$\boldsymbol{m}_\lambda^{(s)} = \boldsymbol{B}_m^{(s)\,\mathrm{T}} \boldsymbol{\lambda}_m \tag{9}$$

To calculate a response to these forces as required for the IBS scheme, they must be transformed into the basis of the impulse response functions $\boldsymbol{H}^{(s)}$, namely the physical space. This is done by inserting the transformation eq. (6), i.e., $\boldsymbol{T}_f^{\mathrm{T}} \boldsymbol{m}$, into eq. (9):

Interface Equilibrium on Virtual Point

$$\underset{\left(n_{\mathrm{I}}^{(s)}\times 1\right)}{\boldsymbol{f}_\lambda^{(s)}} = \underset{\left(n_{\mathrm{I}}^{(s)}\times\left(n_{\mathrm{aI}}^{(s)}+n_{\mathrm{V}}\cdot 6\right)\right)}{\boldsymbol{T}_f^{(s)\,\mathrm{T}}} \quad \underset{\left(\left(n_{\mathrm{aI}}^{(s)}+n_{\mathrm{V}}\cdot 6\right)\times(n_{\mathrm{V}}\cdot 6)\right)}{\boldsymbol{B}_m^{(s)\,\mathrm{T}}} \quad \underset{((n_{\mathrm{V}}\cdot 6)\times 1)}{\boldsymbol{\lambda}_m} \tag{10}$$

where:

n_{I}	Total number of impact locations	n_{V}	Number of Virtual Points	(s)	Substructure index
n_{aI}	Number of additional impact locations	N_S	Total number of substructures		

Adaption of IBS Equations - Lagrange Multiplier Calculation Lastly, the calculation of the Lagrange multipliers must be adjusted. Using the discretization used in [4], this is given as:

$$\left(\sum_{s=1}^{N_S} \boldsymbol{B}_y^{(s)} \boldsymbol{H}^{(s)}[0] \boldsymbol{B}_f^{(s)^{\mathrm{T}}} \right) \boldsymbol{\lambda}_f[k-1] = - \sum_{s=1}^{N_S} \boldsymbol{B}_y^{(s)} \tilde{\boldsymbol{y}}^{(s)}[k] \cdot \frac{1}{\Delta t} \tag{11}$$

On the right-hand side, the compatibility condition is exchanged with the one written for VPT coupling (eq. (8)). On the left-hand side, the interface forces $\boldsymbol{B}_f^{(s)^{\mathrm{T}}} \boldsymbol{\lambda}_f = \boldsymbol{f}_\lambda^{(s)}$ are exchanged with the expression in eq. (10). As the left-hand side would then yield a response due to the Lagrange multipliers in the real space, a premultiplication by the transformation from eq. (4) is necessary to be consistent with the right-hand side, representing the gap in the virtual point coordinates. This yields the new Lagrange multiplier calculation with VPT coupling:

Calculation of Lagrange Multipliers on VPT Interface

$$\left(\sum_{s=1}^{N_S} \boldsymbol{B}_q^{(s)} \boldsymbol{T}_y^{(s)} \boldsymbol{H}^{(s)}[0] \boldsymbol{T}_f^{(s)^{\mathrm{T}}} \boldsymbol{B}_m^{(s)^{\mathrm{T}}} \right) \boldsymbol{\lambda}_m[k-1] = - \sum_{s=1}^{N_S} \boldsymbol{B}_q^{(s)} \boldsymbol{T}_y^{(s)} \tilde{\boldsymbol{y}}^{(s)}[k] \cdot \frac{1}{\Delta t} \tag{12}$$

Discretized IBS Equations with Virtual Point Coupling The only remaining step is to substitute the projection of the VPT interface forces (eq. (10)) into the predictor and corrector step of the IBS scheme. To summarize, the adapted IBS equations with virtual point coupling are given by:

IBS with VPT Predictor Step

$$\tilde{\boldsymbol{y}}^{(s)}[k] = \left(\sum_{i=0}^{k-2} \boldsymbol{H}^{(s)}[k-(i+1)] \left(\boldsymbol{f}^{(s)}[i] + \boldsymbol{T}_f^{(s)^{\mathrm{T}}} \boldsymbol{B}_m^{(s)^{\mathrm{T}}} \boldsymbol{\lambda}_m[i] \right) \Delta t \right) + \boldsymbol{H}^{(s)}[0]\ \boldsymbol{f}^{(s)}[k-1]\ \Delta t \tag{13}$$

Calculation of Lagrange Multipliers on VPT Interface

$$\left(\sum_{s=1}^{N_S} \boldsymbol{B}_q^{(s)} \boldsymbol{T}_y^{(s)} \boldsymbol{H}^{(s)}[0] \boldsymbol{T}_f^{(s)^{\mathrm{T}}} \boldsymbol{B}_m^{(s)^{\mathrm{T}}} \right) \boldsymbol{\lambda}_m[k-1] = - \sum_{s=1}^{N_S} \boldsymbol{B}_q^{(s)} \boldsymbol{T}_y^{(s)} \tilde{\boldsymbol{y}}^{(s)}[k] \cdot \frac{1}{\Delta t} \tag{14}$$

IBS with VPT Corrector Step

$$\boldsymbol{y}_\lambda^{(s)}[k] = \boldsymbol{H}^{(s)}[0] \boldsymbol{T}_f^{(s)^{\mathrm{T}}} \boldsymbol{B}_m^{(s)^{\mathrm{T}}} \boldsymbol{\lambda}_m[k-1]\ \Delta t \tag{15}$$

Sensor and Impact Consistency Criterion When applying the VPT for measurements, various issues could exist, e.g., some impacts are too soft (bad signal-to-noise ratio), or sensor positions, orientations, or calibrations are wrong. Also, the rigid interface assumption will not hold for higher frequencies. Such issues within FBS applications can be detected using the established performance indicators of sensor and impact consistency [5]. Therefore, an adaption for IBS is highly motivated.

The sensor consistency is defined using the response to a unit load case at any excitation dof, which in the frequency domain is represented by a magnitude of one at all frequencies. This essentially extracts the respective column of the FRF matrix [5]. In the time domain, the equivalent of the unit load case is given by a Dirac impulse. Then, the convolution of the IRF matrix with a Dirac impulse at dof i also extracts the i-th column $\boldsymbol{H}_i$ of the IRF matrix $\boldsymbol{H}$. The filtered (time) response $\bar{\boldsymbol{y}}$, i.e., transformed onto the virtual point and back to the physical space, can then be found by substituting eq. (4) in eq. (3):

$$\bar{\boldsymbol{y}} = \boldsymbol{R}_y \boldsymbol{T}_y \boldsymbol{y} = \boldsymbol{R}_y \boldsymbol{T}_y \boldsymbol{H}_i \tag{16}$$

Similarly, the impact consistency uses the response at one sensor channel to all performed impacts, equivalent to one row of the FRF matrix [5], respectively $\boldsymbol{H}_{1i}$ of the IRF matrix. The filtered force $\bar{\boldsymbol{f}}$ is found by substituting eq. (5) in eq. (6):

$$\bar{\boldsymbol{f}} = \boldsymbol{T}_f^{\mathrm{T}} \boldsymbol{R}_f^{\mathrm{T}} \boldsymbol{f} = \boldsymbol{T}_f^{\mathrm{T}} \boldsymbol{R}_f^{\mathrm{T}} \boldsymbol{H}_{1i} \tag{17}$$

In the frequency domain, the criteria for sensor consistency ρ_y^2 and impact consistency ρ_f^2 can be evaluated using a formulation similar to the Modal Assurance Criterion (MAC), giving a value for each frequency [5]:

$$\begin{aligned} \rho_y^2 &= \mathrm{MAC}\left(\bar{\boldsymbol{y}}, \boldsymbol{H}_i\right) \\ \rho_f^2 &= \mathrm{MAC}\left(\bar{\boldsymbol{f}}, \boldsymbol{H}_{1i}\right) \end{aligned} \qquad \text{with} \qquad \mathrm{MAC} = \frac{\left(a^{\mathrm{H}} b\right)\left(b^{\mathrm{H}} a\right)}{\left(a^{\mathrm{H}} a\right)\left(b^{\mathrm{H}} b\right)} \tag{18}$$

However, this evaluation is not as straightforward in the time domain, i.e., in the context of IBS. While applying an FFT and using eq. (18) would be possible, the question is how representative this frequency domain result is. For instance, when only short time signals are used, e.g., only $50\,\mathrm{ms}$, like for the IRFs here, the frequency resolution will be very coarse, and the leakage introduced by the cut-off tremendous. Therefore, a comparison in the time domain should be favored. Nevertheless, the criteria are not further developed here due to the complexity of meaningfully comparing time domain signals of mechanical systems.

Experimental Setup

The substructuring benchmark structure depicted in fig. 4 is used as a test case. The measurements are performed for two physical configurations, once for the assembled system A+B (fig. 4), connected by a bolt with washers torqued to $20\,\mathrm{N\,m}$, and once for the two unconnected substructures A and B (fig. 4). A closer view of the interface is also given in fig. 4. For all configurations, the respective structures are suspended from rubber ropes and can swing freely.

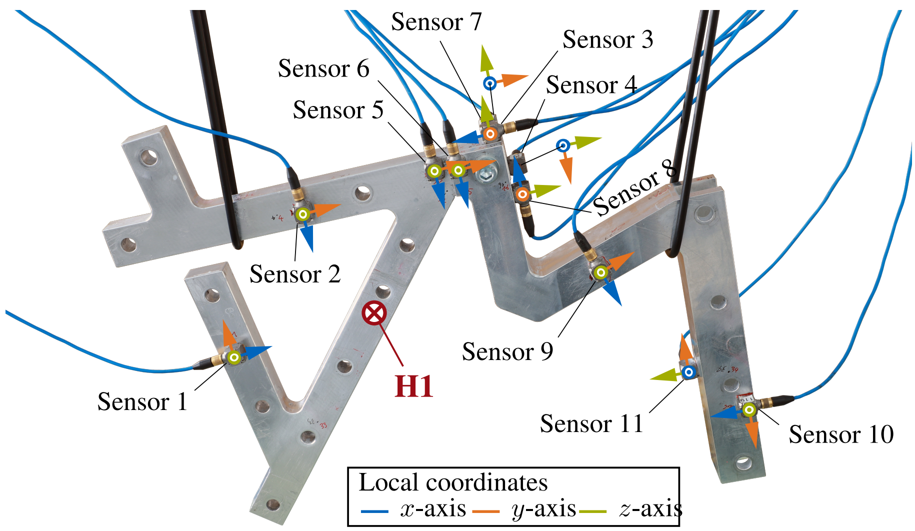

Fig. 4 Experimental setup for the reference measurement of assembled system A+B

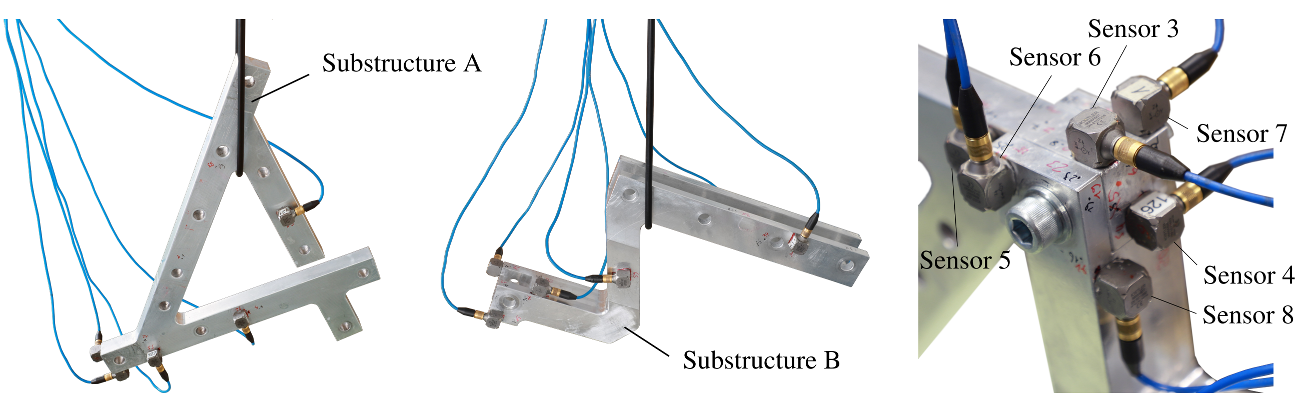

Fig. 5 Experimental setup of individual substructures (left) and interface close-up (right)

The systems are excited using an impact hammer with a vinyl tip. A total of ten impacts are performed per impact location. Accelerations are measured using *KISTLER 8688A50T* triaxial sensors that are glued to the structure. The signals are acquired with a *Müller-BBM PAK MKII* system with a sample rate of $f_S = 102.4\,\mathrm{kHz}$. The sensor as well as impact locations are identical between configurations and are summarized in table 1. The impact locations are described as needed in the following.

Table 1 Summary of utilized sensor and impact locations on the substructuring benchmark structure

	Substructure A		**Substructure B**	
Grouping	Internal	Interface		Internal
Sensors	Sensor 1 & 2	Sensor 3 - 5	Sensor 6 - 8	Sensor 9 - 11
Impacts	H1 - H4 H31 - H33	H5 - H14	H15 - H25[1]	H26 - H30 H34 - H38

IRFs are calculated from the measured signals as described in [4] with a length of $h_{\text{len}} = 50\,\mathrm{ms}$. The required transformation matrices $\boldsymbol{T}_y^{(s)}$ and $\boldsymbol{T}_f^{(s)}$ are generated from sensor and impact positions using *pyFBS* [10]. All measured time series as well as an Excel sheet containing all sensor and impact positions are available for download at: https://doi.org/10.14459/2024mp1754069 [11]. Additionally, a Python script to retrieve the VPT matrices using *pyFBS* is provided.

Experimental Results

For the test setup and sample rate of $f_S = 102.4\,\mathrm{kHz}$ used here, the IBS scheme with VPT immediately becomes unstable, manifesting in the responses and Lagrange multiplier growing toward infinity very quickly. This is because the system excitation is limited and does not excite the whole measurement bandwidth, as already discussed in fig. 2, leading to erroneous high amplitudes in the IRFs at higher frequencies. For illustration, fig. 6 shows the FFT of one averaged experimental IRF.

Fig. 6 Frequency domain view of averaged S1+Z IRF with impact at H1 of substructure A. Vertical lines indicate the cut-off point for a downsampling factor as annotated

As can be seen, the amplitudes around $30\,\mathrm{kHz}$, where basically no excitation above the noise floor exists, are almost two orders of magnitude higher than the peaks in the low-frequency region. Since there is no excitation, the high peaks are most likely only noise that dominates the time domain signal. Because for FBS the substructure assembly is per frequency line, i.e., independent of the FRF content at other frequencies [12], the noisy part does not influence the result at lower frequencies. However, every frequency component is present for IBS at any time (as long as the oscillation did not fully decay). Therefore, this frequency region should not be considered in the IBS scheme and must be removed.

Here, the frequency content is truncated by downsampling (with low-pass filter) the measured signals before estimating the IRFs. Note, however, that the same results could be achieved by reducing the sample rate during the measurements. The IBS results of one combination of sensor channel and impact H1 (see fig. 4) for various downsampling factors are shown in fig. 7.

Since the limits of the shown plots are fixed around the reference measurement, the actual amplitudes of the IBS results cannot be seen from fig. 7; however, they grow to very high values as soon as instability occurs. The instability usually manifests in an oscillation with growing amplitudes between positive and negative numbers.

[1]Note: Impact H21 could not be performed but is retained for consistent numbering

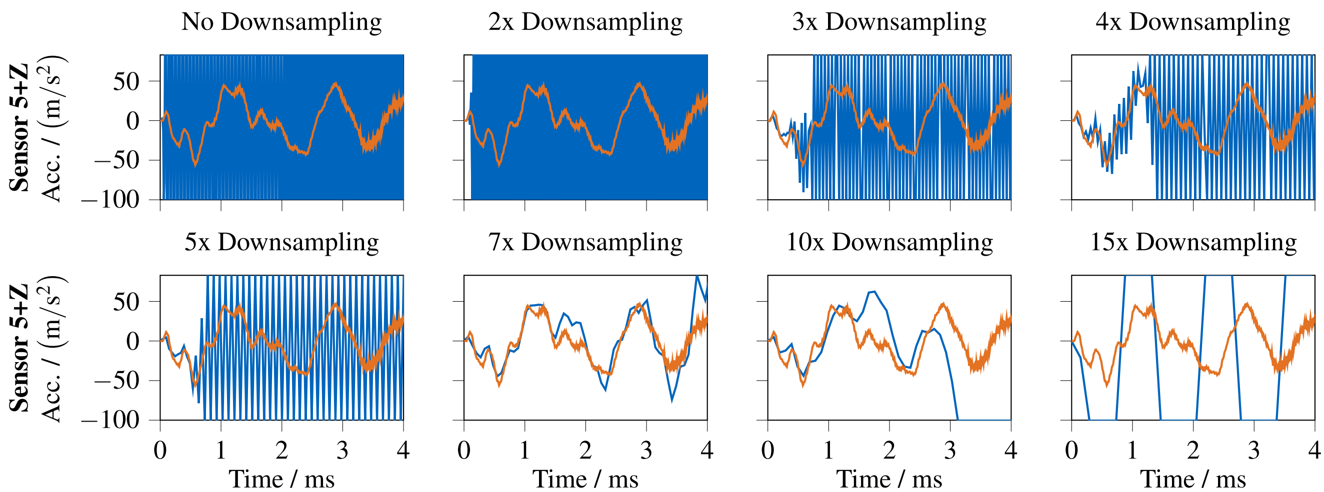

Fig. 7 IBS results of the experimental test case with **excitation at H1** and **response at S5+Z** for various downsampling factors as indicated. Plot limits are fixed around reference measurement amplitudes, — IBS Result, — Measurement

As can be seen, with an increase of the downsampling factor, the instability of the IBS scheme generally decreases. One exception to this is the change from 4x to 5x, where the unstable, high frequent oscillations start to occur sooner than with the lower downsampling factor. The best result can be seen for 7x downsampling, where the IBS result closely matches the reference measurement and then slowly starts to diverge. A further increase of the downsampling factor leads to an earlier divergence, and for 15x, an unstable oscillation can be seen immediately at the start. Using a downsampling factor of 6x or 8x did not produce better results than with 7x downsampling. Therefore, this factor is used in the following.

The IBS results for the other sensors attached to substructure A, specifically, the channels aligned with the impact direction, are shown in fig. 8. For approximately the first millisecond, the IBS results are close to the reference, with a tendency toward overestimation. After that, all responses except the one of Sensor 2+Z show oscillations not present in the measured reference. The response of Sensor 2+Z also becomes unstable and shows growing amplitudes.

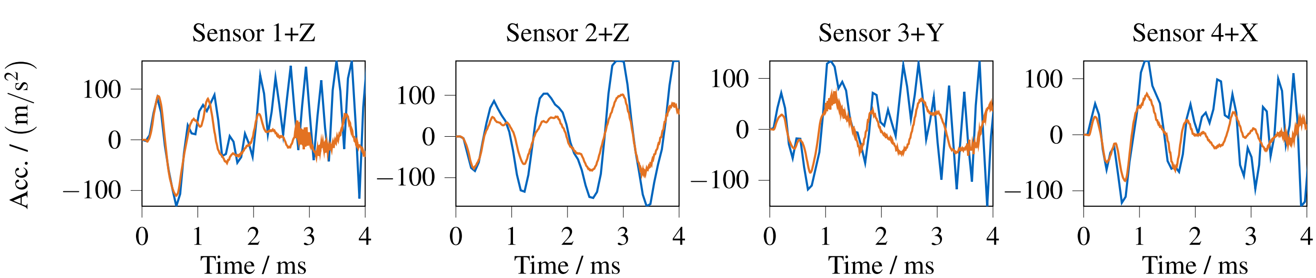

Fig. 8 IBS results of the experimental test case with **excitation at H1** and responses of sensors attached to **substructure A**. Only sensor channels aligned with impact direction are shown. Plot limits fixed, — IBS Result, — Measurement

Responses of some sensors attached to substructure B, i.e., on the other interface side compared to the impact location, are shown in fig. 9; again, only responses in the impact direction are shown. Here, basically, the same observations can be made, where the IBS prediction of the acceleration response is decent in the beginning and then starts to diverge from the reference, which is accompanied by high frequent oscillations for Sensor 8+Y.

The full IBS results, including all sensor channels and the Lagrange multipliers over time, for impact location H1, as well as five other impact locations, can be found in the appendix. For all impacts, there are responses predicted by IBS that match the reference measurement well in the beginning, while other responses do not match the reference or are immediately unstable. Instability manifests in slowly growing amplitudes, high frequent oscillations, or in some cases, e.g., Sensor 1 for impact H26, the responses shoot off toward infinity. In most cases, at least one Lagrange multiplier also steadily grows in amplitude.

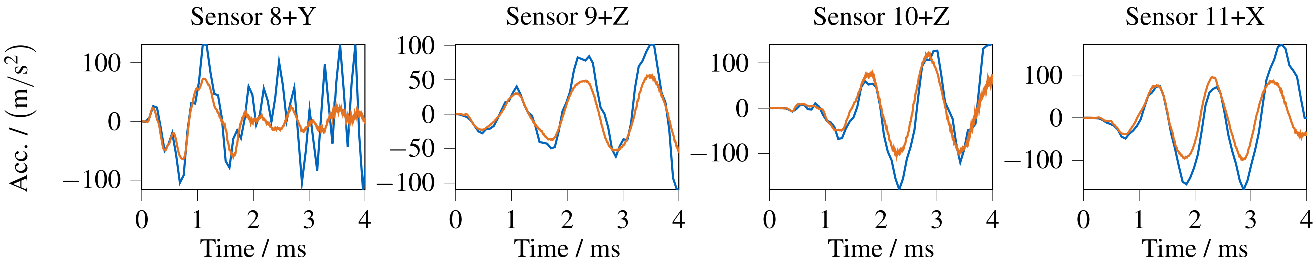

Fig. 9 IBS results of the experimental test case with **excitation at H1** and responses of sensors attached to **substructure B**. Only sensor channels aligned with impact direction are shown. Plot limits fixed, — IBS Result, — Measurement

Here, it is impossible to identify the exact origin of the stability issues. Certainly, errors are introduced by noise, varying impacts, inaccuracies in the IRF estimation, and other typical experimental issues. Since the IBS scheme is based on convolution products, any error will accumulate over time. This implies that at some point, due to unavoidable experimental errors, the IBS scheme will become unstable. Further, any errors in the estimated IRFs will be amplified due to the coupling with Lagrange multipliers; more details are provided in [4]. Using the VPT, the hard enforcement of the interface compatibility is weakened, which should alleviate some of the associated issues already.

Conclusion

In this paper, the theory of the Virtual Point Transformation was incorporated into the discretized equations of the Impulse-Based Substructuring scheme, allowing for an experimental application of IBS on three-dimensional structures. Using time domain deconvolution for estimating the Impulse Response Functions, combined with a reduction of the considered frequency bandwidth using downsampling with a low-pass filter, it was possible to experimentally apply IBS on a substructuring benchmark structure, where the initial acceleration response could be predicted successfully.

Due to some experimental errors, e.g., noise, the IBS scheme becomes unstable after some time. In future works, an improvement of the IRF estimation techniques could potentially lead to a longer amount of the predicted response being stable, i.e., better following the expected response. Nevertheless, the work presented here provides a framework for an experimental application of IBS using the VPT and enables further investigations to improve experimental IBS applications.

References

[1] Gordis, J. H. "Integral equation formulation for transient structural synthesis". In: *AIAA Journal* 33.2 (1995), pp. 320–324. ISSN: 0001-1452. DOI: 10.2514/3.12454.

[2] Rixen, D. J. "Substructuring using Impulse Response Functions for Impact Analysis". In: *Proceedings of the IMAC-XXVIII* (2011). DOI: 10.1007/978-1-4419-9834-7_56.

[3] Rixen, D. J. and Van der Valk, P. L. C. "An Impulse Based Substructuring approach for impact analysis and load case simulations". In: *Journal of Sound and Vibration* 332.26 (2013), pp. 7174–7190. ISSN: 0022-460X. DOI: 10.1016/j.jsv.2013.08.004.

[4] Zobel, O., Trainotti, F., and Rixen, D. "Enabling Experimental Impulse-Based Substructuring Through Time Domain Deconvolution and Downsampling". In: *Experimental Techniques* (2024). ISSN: 1747-1567. DOI: 10.1007/s40799-024-00756-3.

[5] Van der Seijs, M., Bosch, D. van den, Rixen, D., and Klerk, D. *An improved methodology for the virtual point transformation of measured frequency response functions in dynamic substructuring*. 2013. DOI: 10.7712/120113.4816.C1539.

[6] Van Der Seijs, M., Van Der Valk, P., Van Der Horst, T., and Rixen, D. "Towards Dynamic Substructuring Using Measured Impulse Response Functions". In: *Proceedings of the IMAC-XXXII* (2014). DOI: 10.1007/978-3-319-04501-6_6.

[7] de Klerk, D., Rixen, D. J., Voormeeren, S., and Pasteuning, P. "Solving the RDoF problem in experimental dynamic substructuring". In: *Proceedings of the IMAC-XXVI* (2008).

[8] *Virtual Point Transformation - pyFBS documentation*. URL: https://pyfbs.readthedocs.io/en/latest/examples/fbs/virtual_point_transformation.html.

[9] Haeussler, M. and Rixen, D. J. "Optimal Transformation of Frequency Response Functions on Interface Deformation Modes". In: *Dynamics of Coupled Structures, Volume 4*. Cham: Springer International Publishing, 2017, pp. 225–237. ISBN: 978-3-319-54930-9. DOI: 10.1007/978-3-319-54930-9_20.

[10] Bregar, T., Mahmoudi, A. E., Kodrič, M., Ocepek, D., Trainotti, F., Pogačar, M., Göldeli, M., Čepon, G., Boltežar, M., and Rixen, D. J. "pyFBS: A Python package for Frequency Based Substructuring". In: *Journal of Open Source Software* 7.69 (2022), p. 3399. ISSN: 2475-9066. DOI: 10.21105/joss.03399.
[11] Zobel, O. M., Trainotti, F., and Rixen, D. J. *3D Experimental Impulse-Based Substructuring AM Benchmark Structure Measurement Data*. Dataset. 2024. DOI: 10.14459/2024mp1754069.
[12] Allen, M. S., Rixen, D., Seijs, M. van der, Tiso, P., Abrahamsson, T., and Mayes, R. L. *Substructuring in Engineering Dynamics - Emerging Numerical and Experimental Techniques*. 1st ed. Springer Cham, 2020. ISBN: 978-3-030-25532-9. DOI: 10.1007/978-3-030-25532-9.

Appendix: Full IBS Results for Selected Impact Locations

In the following, the full experimental results of the substructuring benchmark structure for selected impacts and 7x down-sampling are shown on double pages, where the responses of substructure A are depicted on the left-hand side and the ones of substructure B on the right-hand side. Additionally, the sensors and the used impact location are shown on the top left of the double pages, and the Lagrange multipliers are on the bottom right.

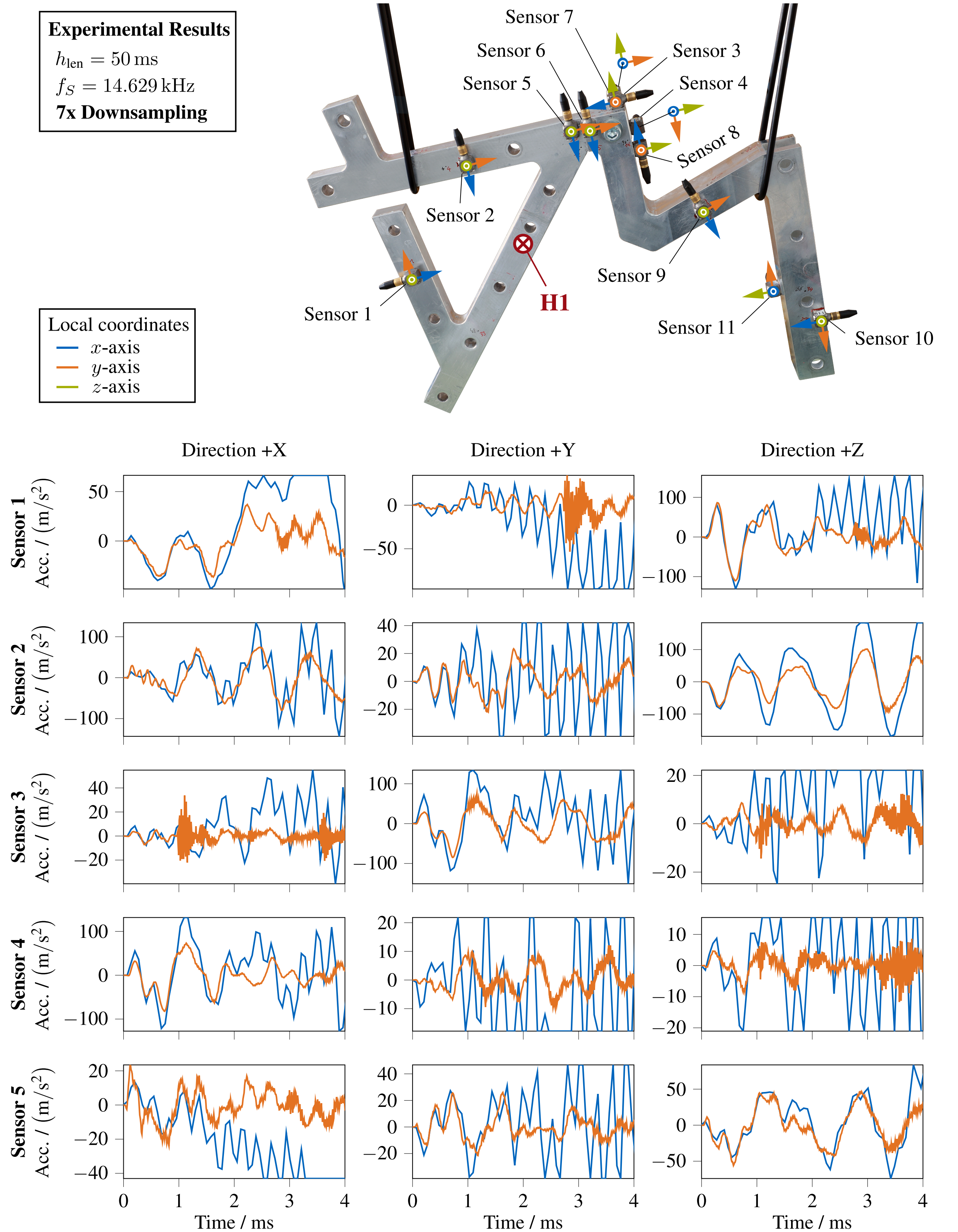

Fig. 10 Experimental IBS results of **Substructure A** sensor dofs for IBS force applied at **impact location H1**, $f_S = 14.629\,\text{kHz}$ (x7 Downsampling), — IBS Result, — Measurement

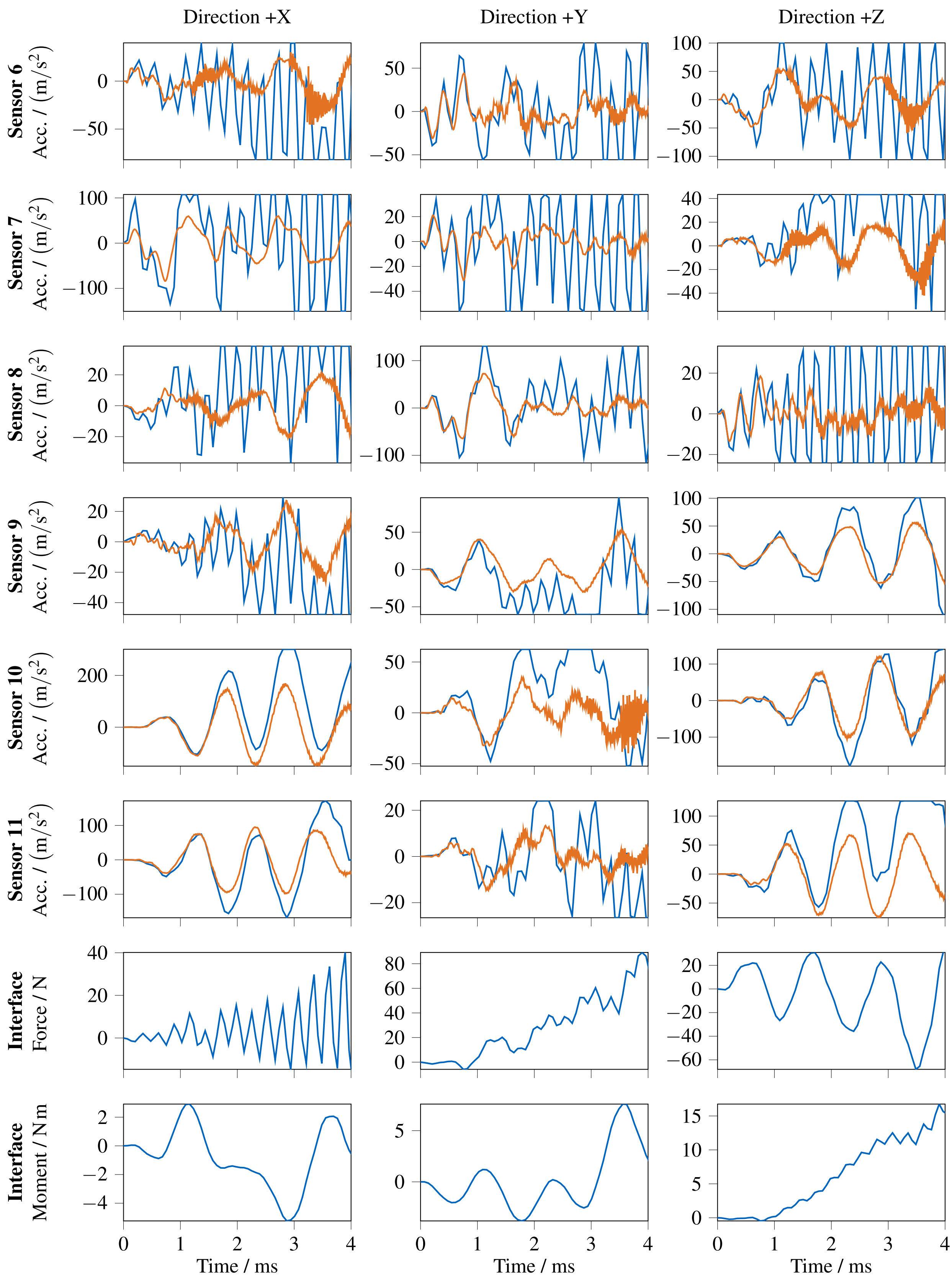

Fig. 11 Experimental IBS results of **Substructure B** sensor dofs and Lagrange multipliers for IBS force applied at **impact location H1**, $f_S = 14.629\,\text{kHz}$ (x7 Downsampling), — IBS Result, — Measurement

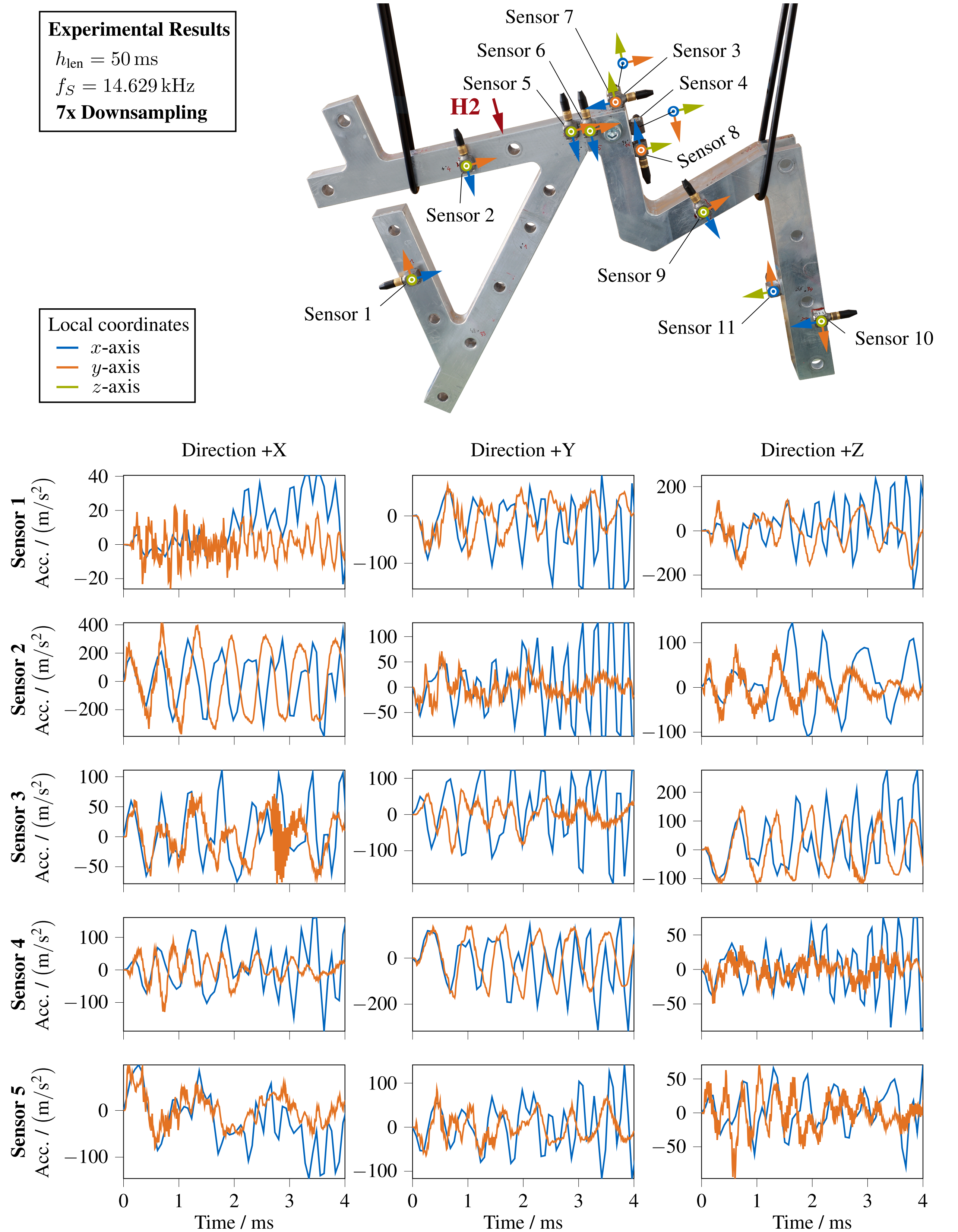

Fig. 12 Experimental IBS results of **Substructure A** sensor dofs for IBS force applied at **impact location H2**, $f_S = 14.629\,\text{kHz}$ (x7 Downsampling), — IBS Result, — Measurement

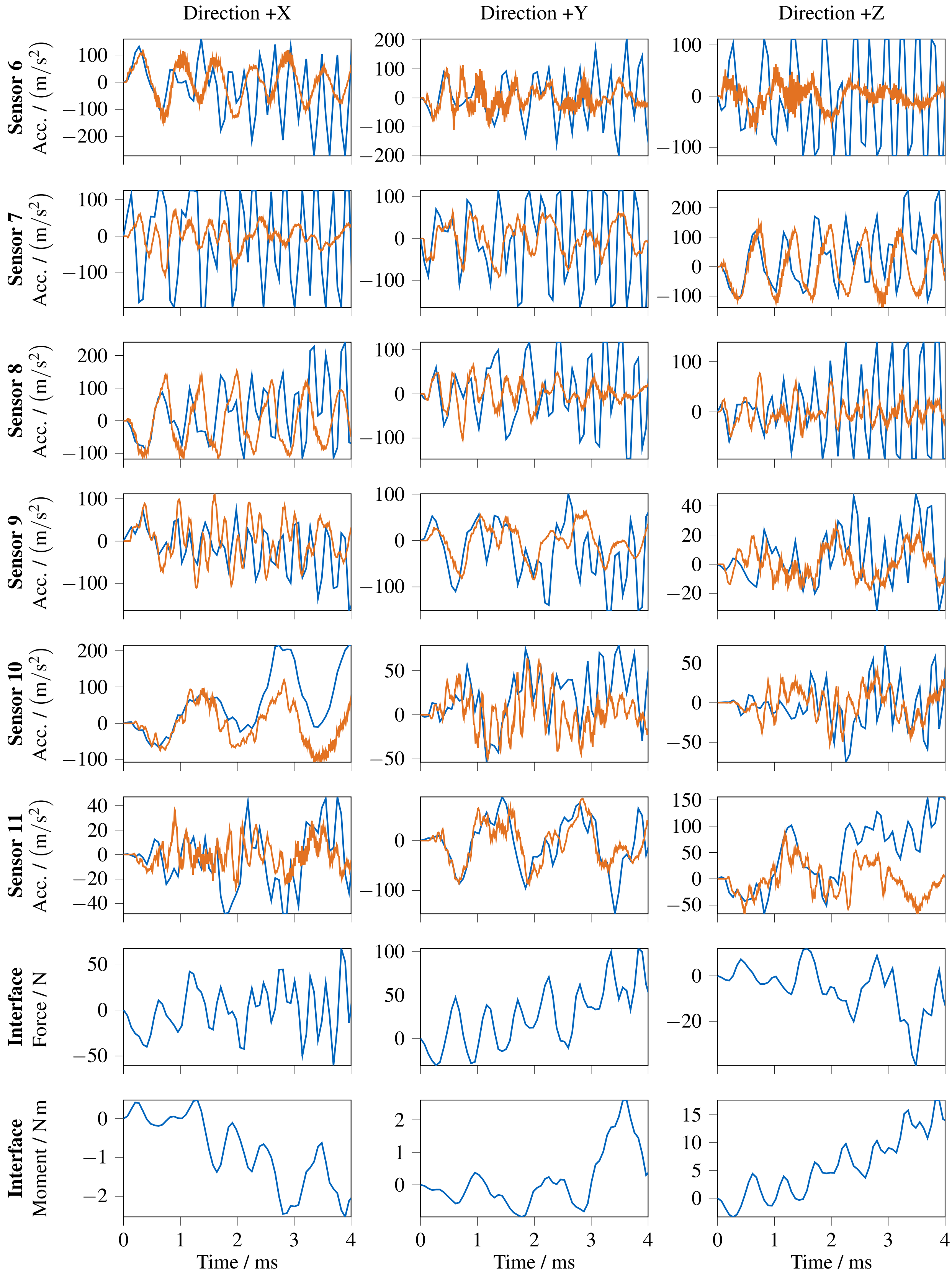

Fig. 13 Experimental IBS results of **Substructure B** sensor dofs and Lagrange multipliers for IBS force applied at **impact location H2**, $f_S = 14.629\,\mathrm{kHz}$ (x7 Downsampling), — IBS Result, — Measurement

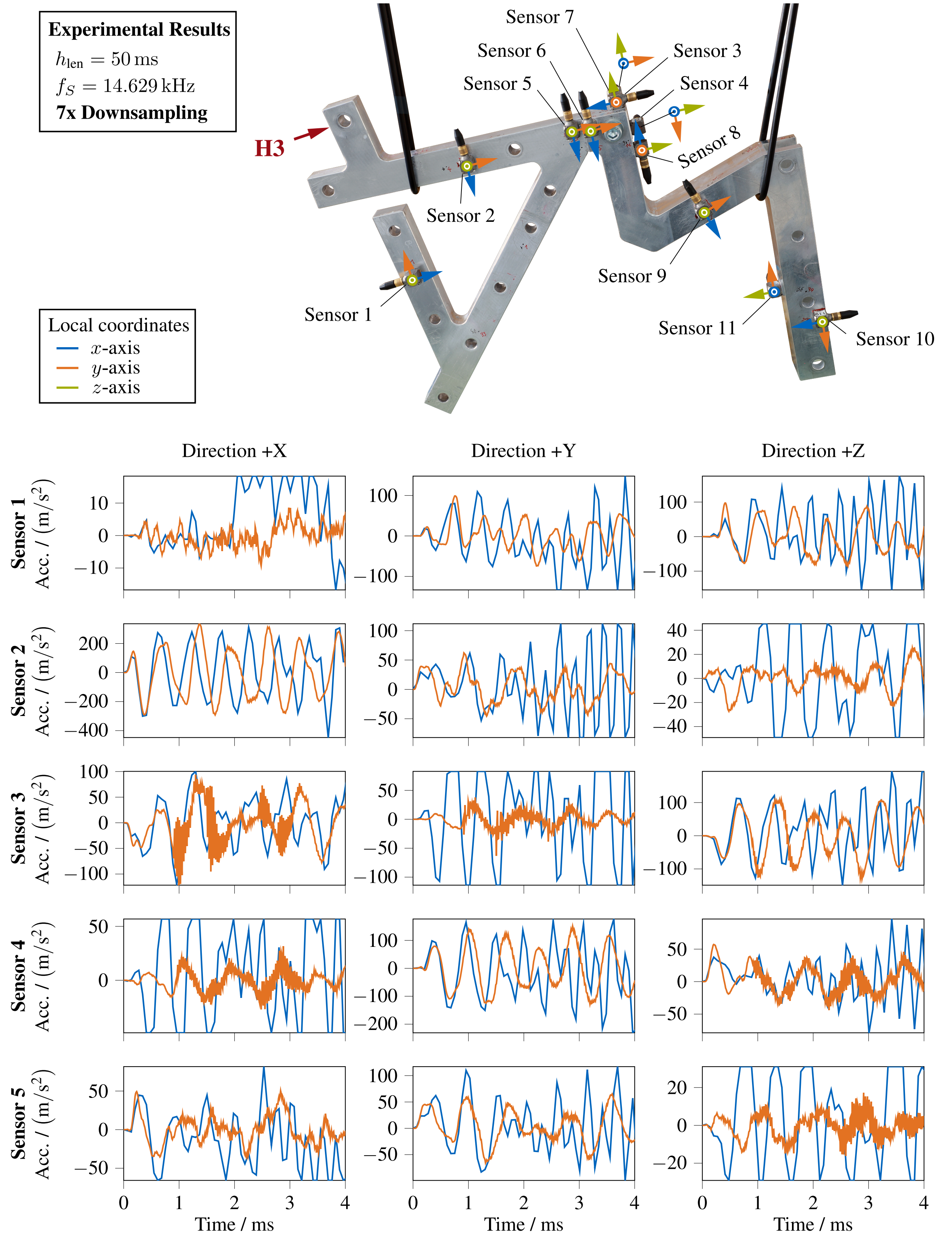

Fig. 14 Experimental IBS results of **Substructure A** sensor dofs for IBS force applied at **impact location H3**, $f_S = 14.629\,\mathrm{kHz}$ (x7 Downsampling), — IBS Result, — Measurement

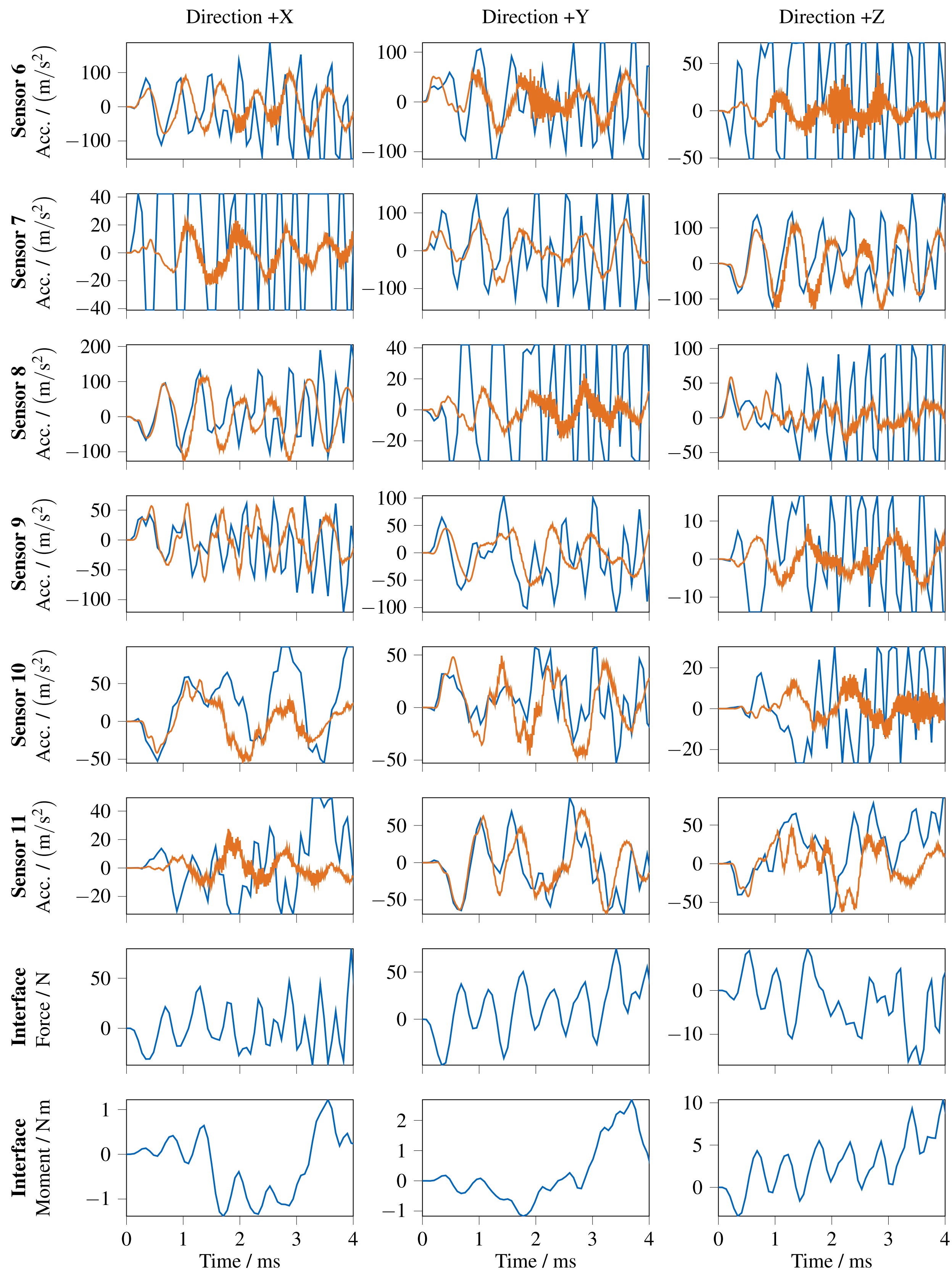

Fig. 15 Experimental IBS results of **Substructure B** sensor dofs and Lagrange multipliers for IBS force applied at **impact location H3**, $f_S = 14.629\,\text{kHz}$ (x7 Downsampling), — IBS Result, — Measurement

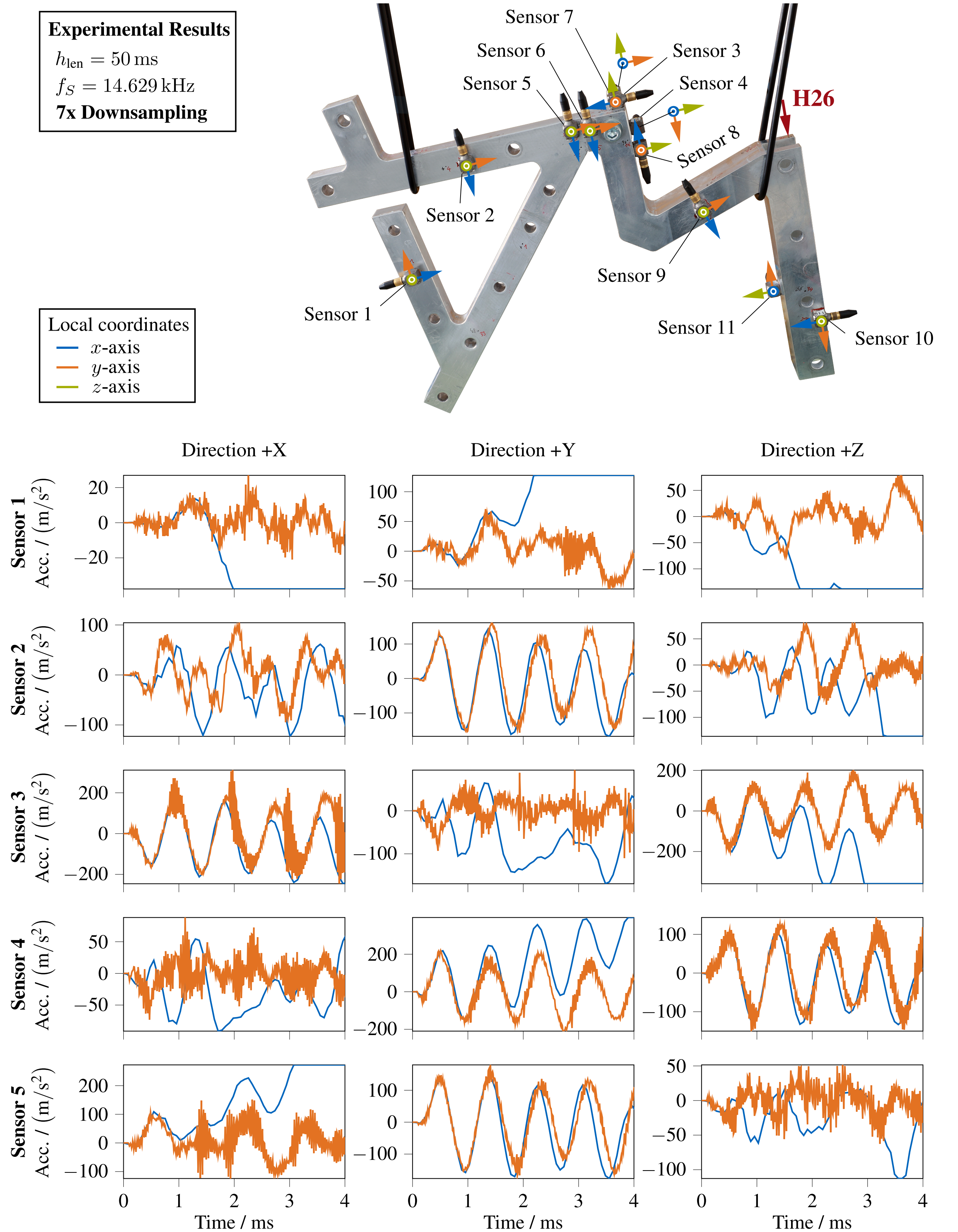

Fig. 16 Experimental IBS results of **Substructure A** sensor dofs for IBS force applied at **impact location H26**, $f_S = 14.629\,\text{kHz}$ (x7 Downsampling), — IBS Result, — Measurement

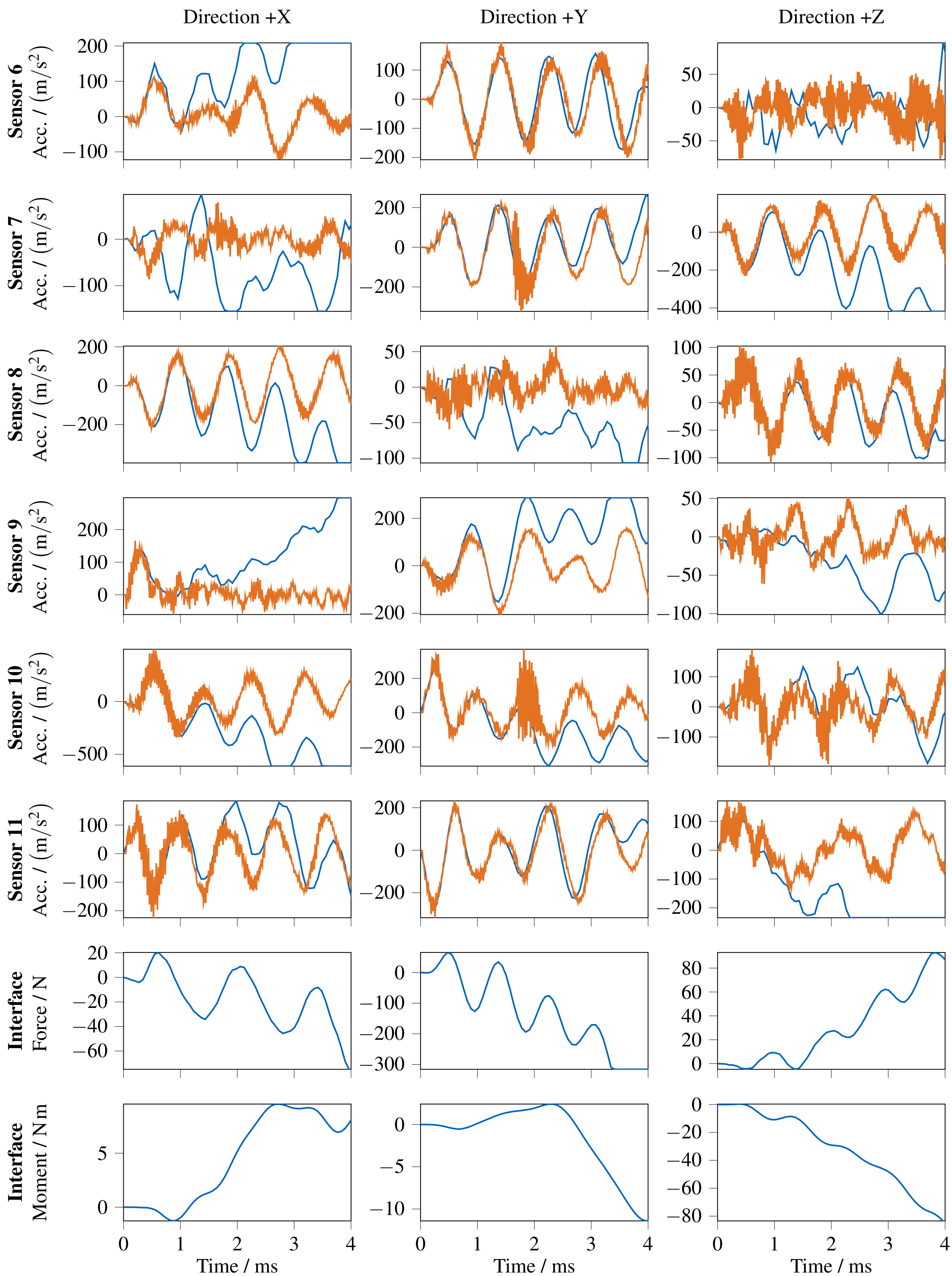

Fig. 17 Experimental IBS results of **Substructure B** sensor dofs and Lagrange multipliers for IBS force applied at **impact location H26**, $f_S = 14.629\,\mathrm{kHz}$ (x7 Downsampling), — IBS Result, — Measurement

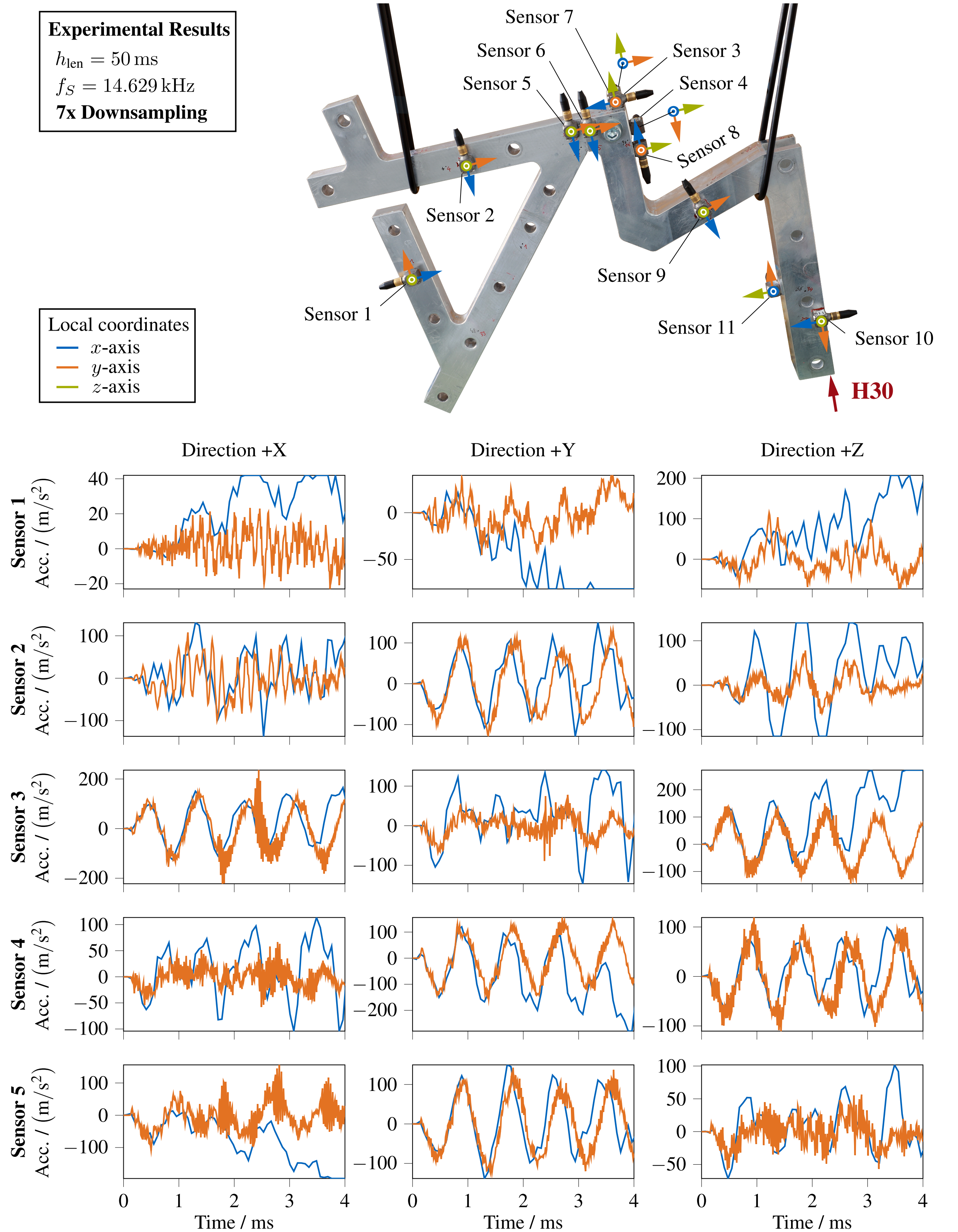

Fig. 18 Experimental IBS results of **Substructure A** sensor dofs for IBS force applied at **impact location H30**, $f_S = 14.629\,\text{kHz}$ (x7 Downsampling), — IBS Result, — Measurement

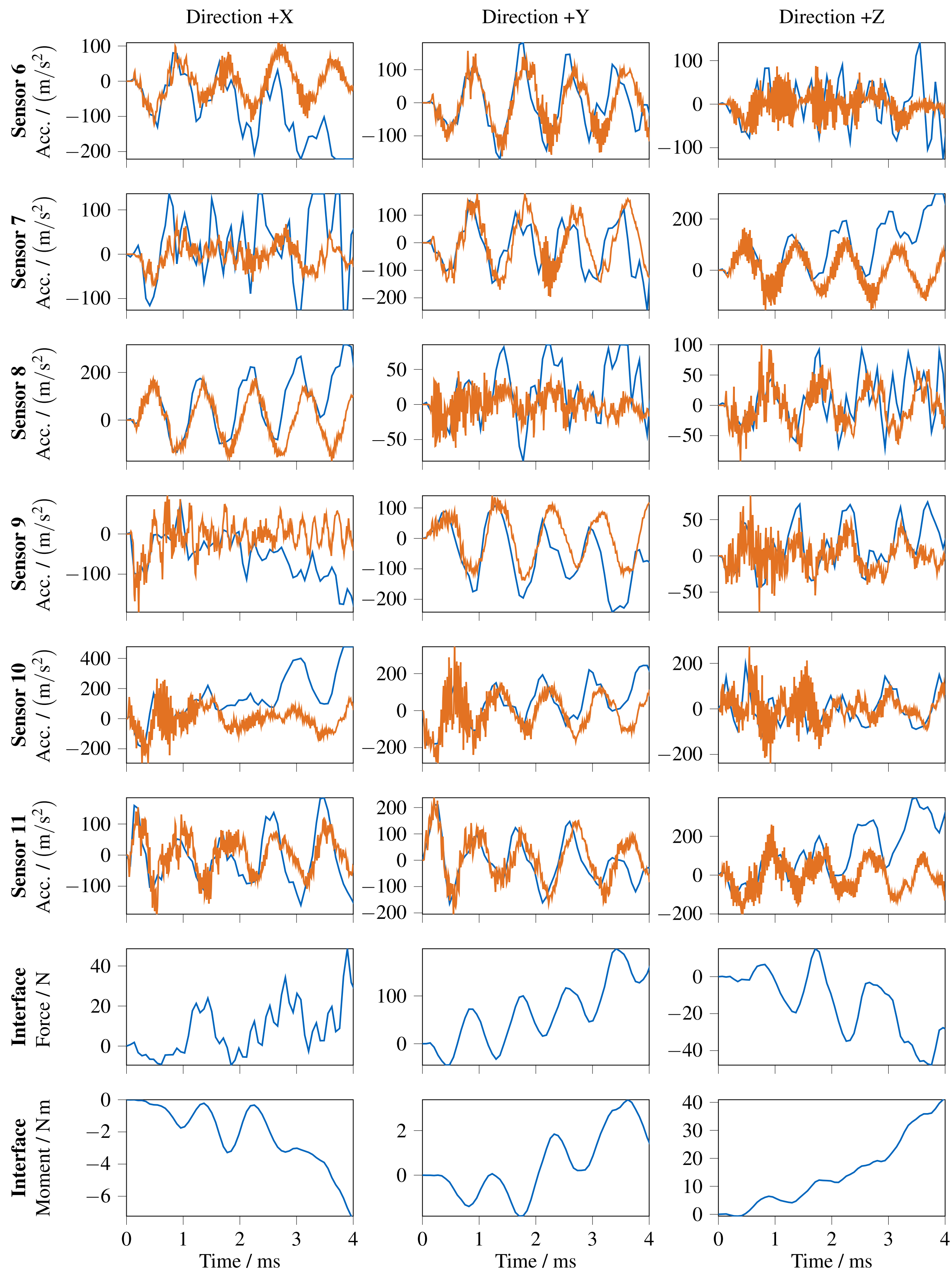

Fig. 19 Experimental IBS results of **Substructure B** sensor dofs and Lagrange multipliers for IBS force applied at **impact location H30**, $f_S = 14.629\,\text{kHz}$ (x7 Downsampling), — IBS Result, — Measurement

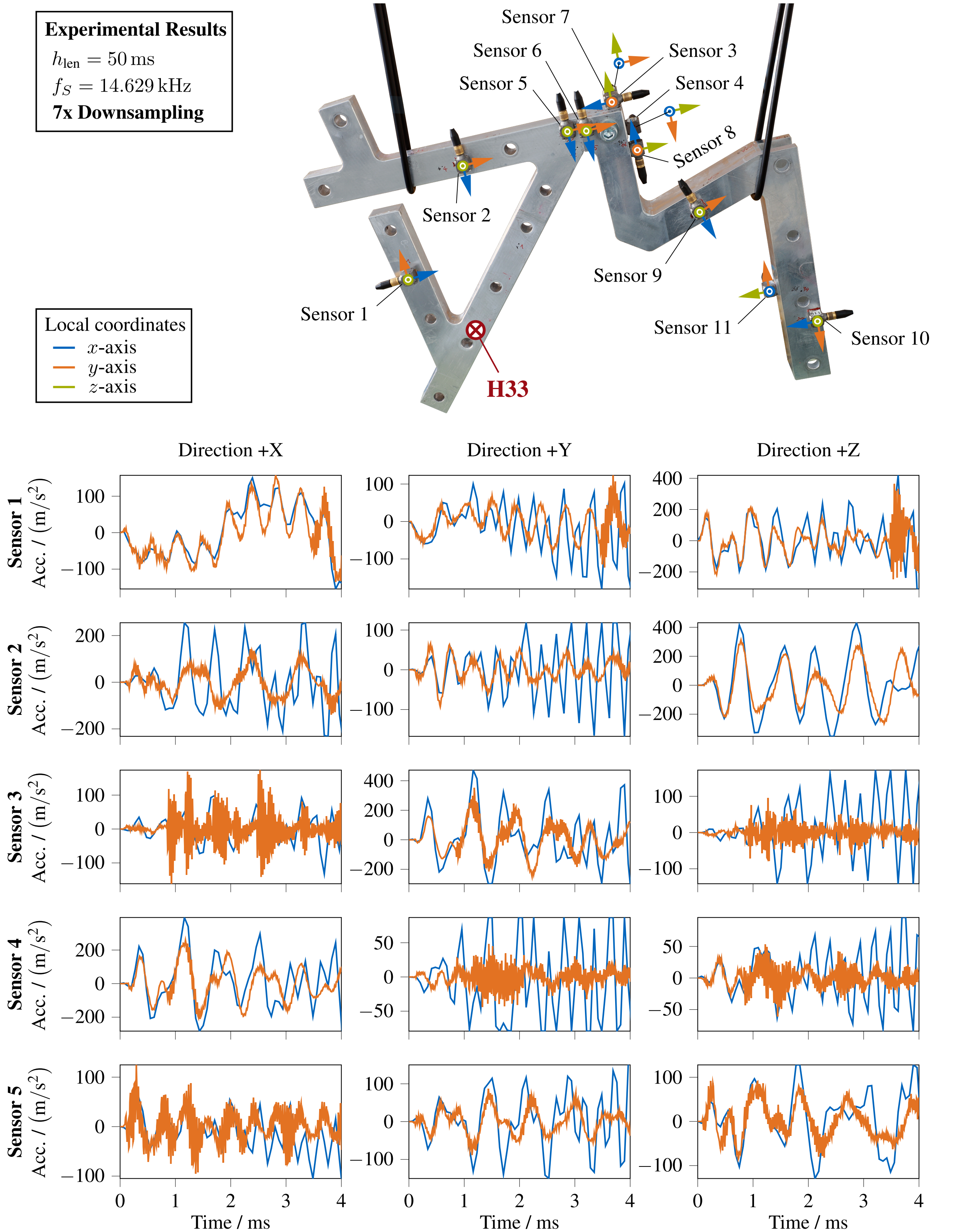

Fig. 20 Experimental IBS results of **Substructure A** sensor dofs for IBS force applied at **impact location H33**, $f_S = 14.629\,\text{kHz}$ (x7 Downsampling), — IBS Result, — Measurement

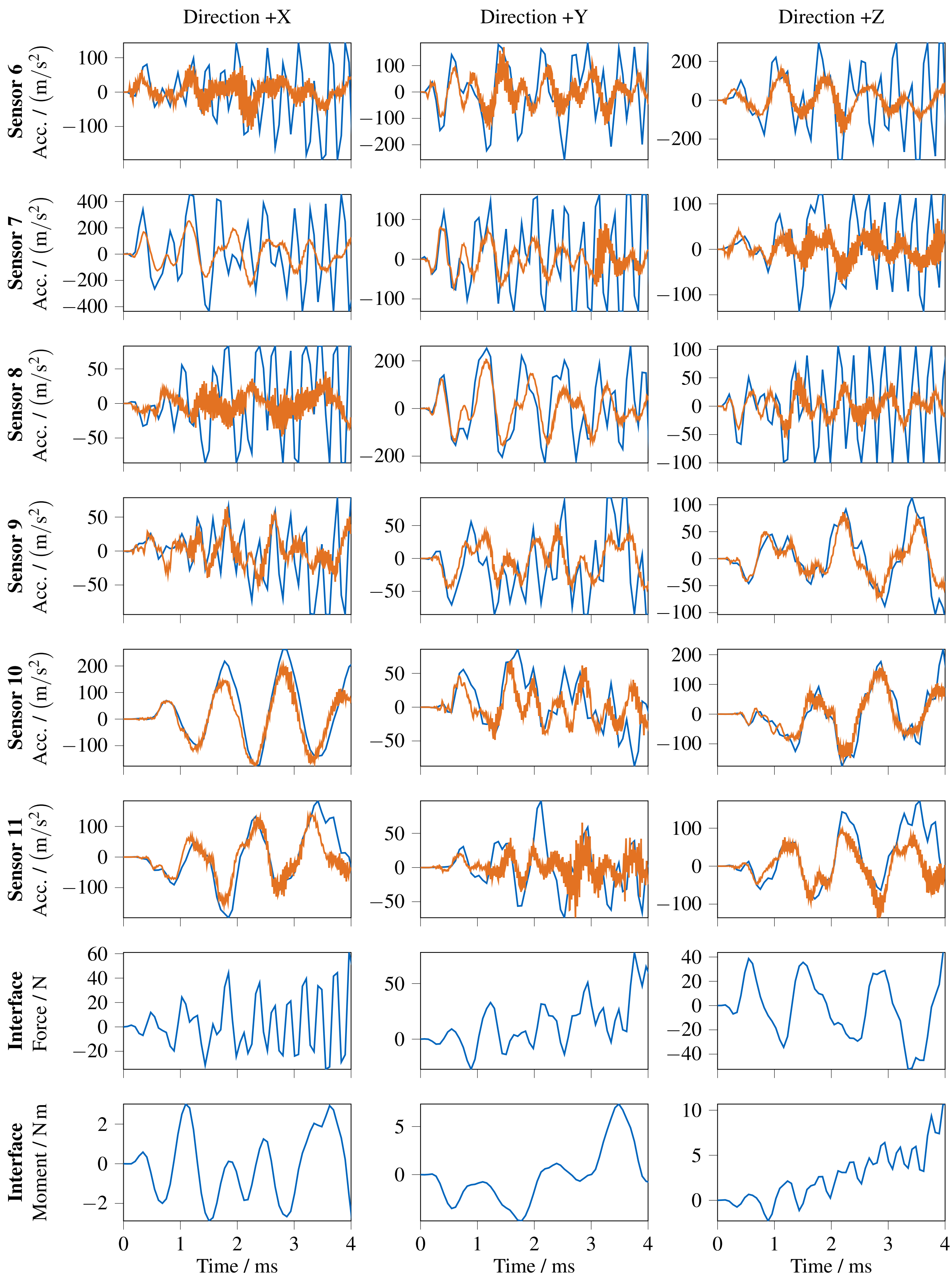

Fig. 21 Experimental IBS results of **Substructure B** sensor dofs and Lagrange multipliers for IBS force applied at **impact location H33**, $f_S = 14.629\,\text{kHz}$ (x7 Downsampling), — IBS Result, — Measurement